nature nanotechnology

Article

https://doi.org/10.1038/s41565-023-01360-z

Leaky-wave metasurfaces for integrated photonics

Received: 18 July 2022

Accepted: 22 February 2023

Published online: 8 May 2023

Check for updates

Heqing Huang[1,4], Adam C. Overvig[1,2,4], Yuan Xu[1], Stephanie C. Malek[1], Cheng-Chia Tsai[1], Andrea Alù[2,3] ✉ & Nanfang Yu[1] ✉

Metasurfaces have been rapidly advancing our command over the many degrees of freedom of light; however, so far, they have been mostly limited to manipulating light in free space. Metasurfaces integrated on top of guided-wave photonic systems have been explored to control the scattering of light off-chip with enhanced functionalities—namely, the point-by-point manipulation of amplitude, phase or polarization. However, these efforts have so far been limited to controlling one or two optical degrees of freedom at best, as well as device configurations much more complex compared with conventional grating couplers. Here we introduce leaky-wave metasurfaces, which are based on symmetry-broken photonic crystal slabs that support quasi-bound states in the continuum. This platform has a compact form factor equivalent to the one of grating couplers, but it provides full command over the amplitude, phase and polarization (four optical degrees of freedom) across large apertures. We present devices for phase and amplitude control at a fixed polarization state, and devices controlling all the four optical degrees of freedom for operation at a wavelength of 1.55 μm. Merging the fields of guided and free-space optics through the hybrid nature of quasi-bound states in the continuum, our leaky-wave metasurfaces may find applications in imaging, communications, augmented reality, quantum optics, LIDAR and integrated photonic systems.

A monochromatic optical wavefront in free space is characterized by four degrees of freedom at each point in space, namely, (A, Φ, ψ, χ): the amplitude A, phase Φ and polarization state with elliptical parameters ψ and χ representing the polarization orientation and ellipticity, respectively. The manipulation of these degrees of freedom is among the key goals of contemporary photonics research. Metasurfaces[1–3]—flat optical devices composed of arrays of subwavelength scatterers—have been offering a flexible and powerful platform for producing desired wavefronts starting from unpatterned plane waves incident from free space[4]. Metasurfaces at optical frequencies have been widely used to spatially manipulate the phase, but have also been shown to manipulate the phase and amplitude (PA)[5,6], phase and polarization state[7,8], and recently all the four parameters simultaneously[9–12] and beyond[13]. These concepts can be leveraged to an even larger extent in the radio-frequency (RF) spectrum, for which multilayered fabrication and the large conductivity of metals enable exquisite and deeply subwavelength control of electromagnetic radiation[14–18]. In addition to free-space excitation, RF leaky-wave antennas[19–21] have been developed over several decades[22] to produce free-space beams by scattering radiation originating from guided modes. Metasurface concepts have recently advanced this field[23–27], but these approaches are not straightforwardly transferable to optical frequencies. For comparison, grating couplers (GCs) in integrated photonics also generate free-space light from in-plane guided sources, but are largely limited in controlling the optical degrees of freedom (A, Φ, ψ, χ) and their spatial profile.

[1]Department of Applied Physics and Applied Mathematics, Columbia University, New York, NY, USA. [2]Photonics Initiative, Advanced Science Research Center, City University of New York, New York, NY, USA. [3]Physics Program, Graduate Center of the City University of New York, New York, NY, USA. [4]These authors contributed equally: Heqing Huang, Adam C. Overvig. ✉e-mail: aalu@gc.cuny.edu; ny2214@columbia.edu

https://doi.org/10.1038/s41565-023-01360-z

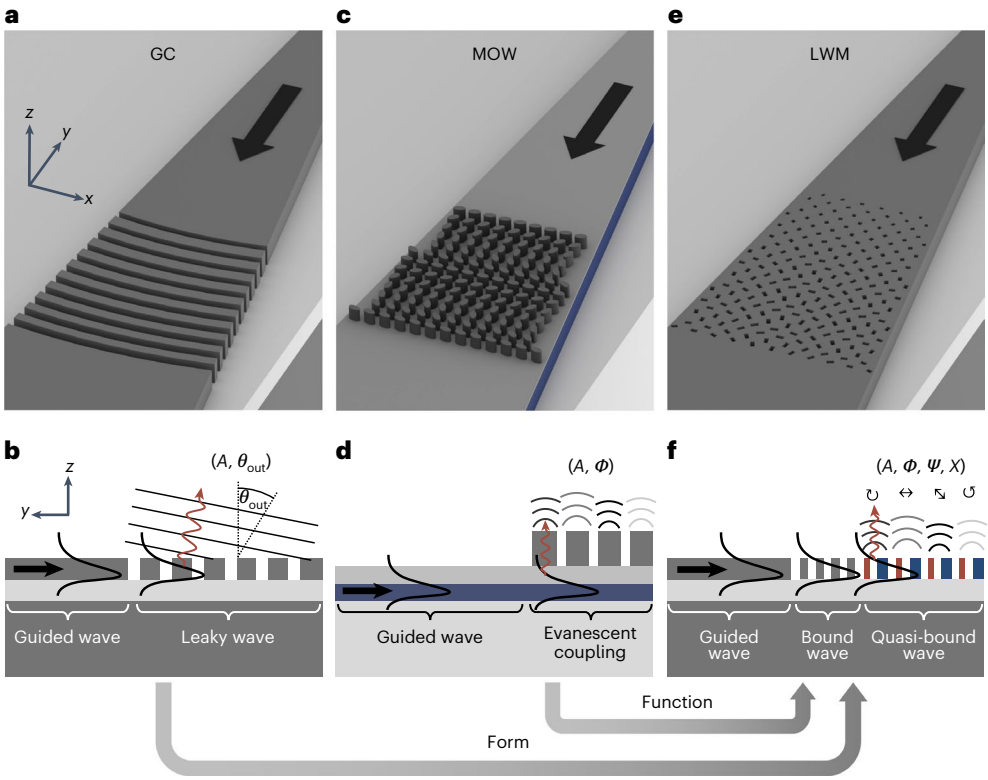

Fig. 1 | Out-coupling in integrated photonic devices. a, Schematic of a typical GC based on a fully etched waveguide grating. **b**, Side view showing the functionality of a conventional GC, where the duty cycle and period may be changed to alter the amplitude and outgoing angle. **c**, Schematic of a metasurface-on-waveguide (MOW) device, based on a high-dielectric-constant pillar array on a waveguide layer (blue). **d**, Side view showing the functionality of the MOW, where the metasurface scatters the evanescent component of a guided wave into the far field, typically limited to the control of two optical parameters of surface emission. **e**, Schematic of the LWM platform introduced in this work, in which a perturbed (that is, symmetry-broken) subwavelength photonic crystal slab supports a tailored quasi-bound wave controlling off-chip coupling. **f**, Side view showing that the LWM has a compact form equivalent to a GC, but more advanced functionality compared with the MOW, offering simultaneous control over all the four degrees of freedom of light (A, Φ, ψ, χ).

Recent years have seen a rapidly growing interest in incorporating metasurface principles into integrated photonics[28,29] and, very recently, in generating wavefronts from one-dimensional[30,31] or two-dimensional[32–38] in-plane guided modes. This capability is of great interest to the broader optics community, opening opportunities to control the off-chip emission of customized free-space wavefronts, as well as leveraging the on-chip manipulation of light based on the commercially maturing field of photonic integrated circuits (PICs). The customizability of a metasurface-based replacement for GCs offers exciting opportunities for optical communications, augmented reality, quantum optics and LIDAR. However, so far, the presented approaches offer only partial solutions, not capable of fully controlling the coupling of guided waves to far-field radiation. Typically, only one[32–34] or two[35–38] optical degrees of freedom have been manipulated at once for a given guided wave, limiting applications to scalar fields (Supplementary Table 1 lists the recent progress made in this context).

Additionally, contrary to corrugated structures typically seen in GCs used in integrated photonics (Fig. 1a,b), the structures proposed so far are composed of a waveguiding layer and a metasurface as two separate objects (Fig. 1c,d), which hinders integrability, scalability and compactness. In early examples, separated metasurface and GC layers were used[39], whereas in more recent examples, the metasurface was placed in the evanescent field of the guided mode to both scatter light and manipulate its phase profile. Both metallic[30] and dielectric[33] structures have been explored, introducing either optical loss or high-aspect-ratio dielectric structures typical of metasurface approaches. Adding such a lossy or high-aspect-ratio metasurface layer on top of existing waveguiding structures complicates its implementation compared with conventional GCs. Additionally, so far, these efforts have been limited to small surface emission apertures. These factors hinder the adoption of this approach in PICs. In contrast, a device configuration featuring the compact form factor typical of GCs, and capable of robust, subwavelength control of all the four degrees of freedom of light (A, Φ, ψ, χ) introduces a generalization (and where appropriate, replacement) of GCs, advancing existing approaches in both form and function.

In this work, we introduce a leaky-wave metasurface (LWM) platform based on weakly corrugated, symmetry-broken photonic crystal slabs, which supports a quasi-bound wave capable of arbitrarily tailoring the scattered field (A, Φ, ψ, χ) with subwavelength resolution (Fig. 1e,f). LWMs inherit the form of GCs and greatly improve the functionality of metasurface-on-waveguide solutions. We experimentally implement the proposed concepts in the near-infrared spectral region (near $\lambda = 1.55$ μm) based on a silicon nitride (Si_3N_4) and polymer system, where nanostructured polymer zones on an unpatterned Si_3N_4 thin film define both rib waveguides and LWMs. The design principles are rooted in quasi-bound states in the continuum[40,41] and diffractive non-local metasurfaces[41–45], enabling a rational design approach with largely independent mapping of four geometric parameters to the four optical degrees of freedom. To demonstrate the flexibility of our platform, we realize the focused emission of a desired linear polarization (with wavelength-tuned scanning of the focal spot), a vortex beam generated in concert with a Gaussian reference beam, a two-image hologram encoded in the amplitude and phase of a single polarization, a four-image hologram encoded in the amplitudes and phases of two orthogonal polarizations, and a converging Poincaré beam[46].

https://doi.org/10.1038/s41565-023-01360-z

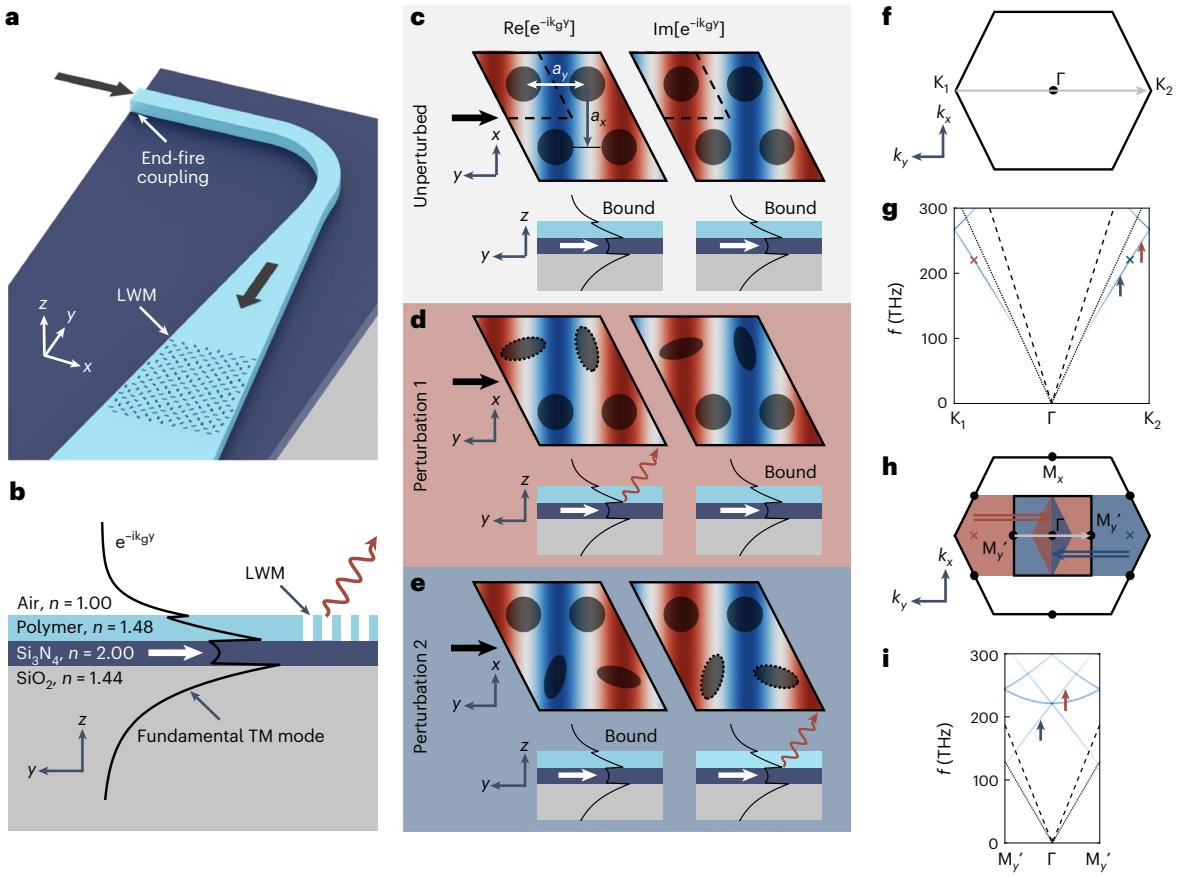

Fig. 2 | Perturbative scheme for rationally designed LWMs. a,**b**, Schematic (**a**) and side view (**b**) of the device geometry. **c**–**e**, Perturbative scheme for the simultaneous control of the real and imaginary components of the out-of-plane scattered wave. In the unperturbed structure (**c**), both real and imaginary components are bound. When the top (bottom) row of circles is perturbed into ellipses (denoted by the black dashed boundaries), the real (imaginary) part of the quasi-bound wave is coupled to free space, but the imaginary (real) part is not (**d** and **e**). **f**,**g**, First Brillouin zone (**f**) and TM band diagram (**g**) of the unperturbed structure. **h**,**i**, First Brillouin zone (**h**) and TM band diagram (**i**) of the perturbed structure, supporting a zone-folded Dirac point. The modes marked by the arrows in **i** correspond to those in **g**, and the red and blue crosses marked in **h** correspond to those in **g**. The dotted and dashed lines in **g** and **i** denote the light cones in the substrate (glass) and superstrate (air), respectively.

Operating principles and metasurface design

The key operating principle of our LWM platform is the deliberate perturbation of a guided mode supported by a periodic structure with subwavelength pitch (that is, a bound wave under the light line) into a quasi-bound wave (above the light line). As sketched in Fig. 1f, a guided mode incident from a waveguide couples to a bound wave in the subwavelength periodic structure, which then leaks into free space due to a period-doubling perturbation[47]. As a proof of principle, we use the configuration shown in Fig. 2a,b based on a rib waveguide and a metasurface defined within a thin layer of polymer ($n \approx 1.48$) atop an unpatterned thin film of Si_3N_4 ($n \approx 2.00$) sitting on a silicon dioxide substrate ($n \approx 1.44$) (Methods provides the detailed geometrical parameters). The metasurface in its unperturbed state (Fig. 2c) is a two-dimensional photonic crystal composed of an oblique lattice of circular holes with pitches a_x and a_y; it supports a bound wave travelling in the $-y$ direction, whose effective wavelength is approximately $\lambda_{\text{eff}} \approx 2a_y$. Two independent perturbations are applied to the top pair of circular holes (Fig. 2d, Perturbation 1) and to the bottom pair of circular holes (Fig. 2e, Perturbation 2). These perturbations double the effective lattice pitches to $2a_x$ and $2a_y$ and alter the lattice from oblique to rectangular (Supplementary Section 2), modifying the first Brillouin zone of the unperturbed lattice (Fig. 2f) and its band diagram (Fig. 2g) into the zone-folded versions (Fig. 2h,i). The resulting band structure supports transverse-magnetic (TM) modes near $\lambda_{\text{eff}} \approx 2a_y$ in the form of a Dirac point at normal incidence, allowing operation anywhere at or near normal to the device plane[48]. We note that an undesirable flat band also arises, degenerate with the Dirac point when $a_x = a_y$, which may be blueshifted or redshifted by detuning from this condition, if desired (Supplementary Section 3). In this way, the deliberate engineering of the symmetry-breaking perturbation (Fig. 2) determines both if and how the wave leaks into free space, at or near the device normal and pixel by pixel across the LWM aperture.

The dual-perturbation scheme (Fig. 2d,e) enables the independent control of the real and imaginary parts of the scattered light, which together confer complete command over the surface emission: (A, Φ, ψ, χ). Here we choose the fundamental TM guided mode (Fig. 2b), which—once coupled into the unperturbed subwavelength lattice—is decomposed into its real and imaginary components (Fig. 2c). Each of these components of the travelling TM wave (characterized in the y direction by e^{-iky}) is a standing wave of either even or odd parity in the y direction (that is, cosine or sine). These standing waves abide by the selection rules for scattering near the device normal, determining which polarization (if any) couples to free space due to the symmetries broken by the perturbation[41]. The real component is bound except in the presence of Perturbation 1, where the top pair of circles are perturbed into ellipses oriented 90° relative to one another (Fig. 2d, dashed boundaries). However, Perturbation 1 does not affect the imaginary component, which is symmetry-protected due to its

https://doi.org/10.1038/s41565-023-01360-z

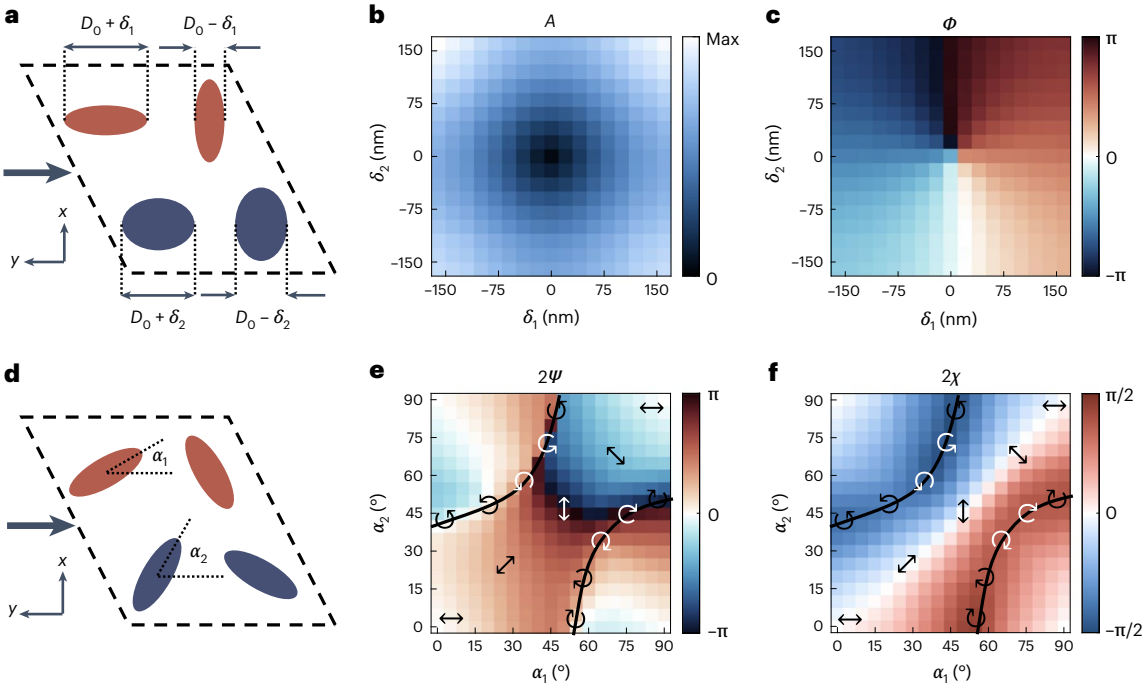

Fig. 3 | Full-wave simulations constructing the meta-unit library. a, For fixed elliptical orientations, perturbations δ_1 and δ_2 determine the signed magnitude of the real and imaginary parts of the scattered field, respectively. **b**, Map of the scattered amplitude of *y*-polarized light as a function of δ_1 and δ_2, showing a bound state when both perturbations vanish. **c**, Map of the scattered phase of *y*-polarized light as a function of δ_1 and δ_2, supporting a topological feature characteristic of a geometric phase. **d**, For fixed δ_1 and δ_2, perturbation angles α_1 and α_2 determine the polarization state scattered by the unit cell. **e**,**f**, Map of 2ψ (**e**) and 2χ (**f**) as a function of α_1 and α_2, where the dashed contours denote the chiral states near the poles of the Poincaré sphere. The arrows denoting the approximate polarization states are overlaid for reference.

opposite parity. Perturbation 2 has exactly the opposite effect for the same reason: the imaginary component is scattered, whereas the real component is not (Fig. 2e). Supplementary Section 5 discusses these selection rules in more detail.

The behaviour of a meta-unit can be analytically modelled in combination with full-wave simulations (Methods). Figure 3a shows two geometric degrees of freedom, δ_1 and δ_2, which determine the sign and strength of each perturbation and hence the signed magnitude of the real and imaginary components of the scattered light. Figure 3b,c shows the amplitude and phase of the scattered light (*y* polarized in this case), respectively. At the origin ($\delta_1 = \delta_2 = 0$), a singularity is observed in the phase, corresponding to a null in the scattering amplitude, that is, a bound wave due to the absence of perturbation. This topological feature is a manifestation of the polarization-agnostic geometric phase recently demonstrated to control Fano resonances in non-local metasurfaces[49]. Here we leverage this principle to enable LWMs with complete PA control of any polarization. To produce scattered light with other polarization states, the orientation angles α_1 and α_2 of the ellipses may be varied (Fig. 3d). Figure 3e,f shows elliptical parameters ψ and χ of the scattered light as a function of α_1 and α_2, with example polarization states drawn for reference; between the dashed contours, arbitrary elliptical polarization states are possible. Collectively, by varying the geometric parameters ($\delta_1, \delta_2, \alpha_1, \alpha_2$), we can arbitrarily specify the scattered state (A, Φ, ψ, χ). The mapping between these parameter spaces, including fine adjustments based on full-wave simulations, are discussed in Methods. As a result, we obtain a semi-analytical library of meta-units for use in populating an LWM that—on excitation with a guided wave—produces free-space radiation with the desired spatial profiles of amplitude, phase and polarization.

Finally, the PA distributions of the guided portion of the quasi-bound wave must be accounted for when populating the LWM with meta-units targeting a specific device function (Methods). For instance, Fig. 4a shows a target PA profile producing a focused beam and Fig. 4b shows the mode-corrected PA profile, adjusted based on the guided mode depicted in Fig. 4c. Hence, targeting *y*-polarized light, Fig. 4d,e shows the resulting profiles of δ_1 and δ_2. The LWM design was then fabricated using electron-beam lithography and characterized in the near-infrared spectral region (Methods). An example photograph and a scanning electron micrograph of the fabricated devices are shown in Fig. 4f,g.

PA control

We experimentally demonstrate the ability of our LWM platform to generate custom PA wavefronts, choosing meta-unit motifs with fixed angles α_1 and α_2 such that the wavefronts are linearly polarized. For *y*-polarized surface emission, we choose $\alpha_1 = \alpha_2 = 0°$, whereas for *x*-polarized surface emission, we choose $\alpha_1 = \alpha_2 = 45°$ (Fig. 3e). Figure 5 shows four examples of LWMs, demonstrating focusing, generation of orbital angular momentum (OAM), PA holography and generation of a kagome lattice.

First, Fig. 5a shows a schematic of an LWM generating a converging beam in the surface-normal direction. As shown in Fig. 4a, a Gaussian envelope is applied to the device's amplitude profile, and the phase profile of a metalens is encoded to focus light at a target focal length of $f = 2$ mm (numerical aperture (NA) ≈ 0.1). Longitudinal cross sections of the beam are shown in Fig. 5b,c, at $\lambda = 1{,}530$ nm, whereas a transverse cross section at the focal plane is shown in Fig. 5d, where a focal spot is observed with full-width at half-maximum values of $w_x = 10.0 \pm 0.3$ μm in the *x* direction and $w_y = 9.1 \pm 0.1$ μm in the *y* direction. These values are in good agreement with diffraction-limited operation, with simulated values $w_x = 9.1$ μm and $w_y = 9.4$ μm (Fig. 5d, insets). Images of the focal plane at various operating wavelengths from 1,520 to 1,580 nm are shown in Fig. 5e. The position of the focal spot along the *y* direction shifts linearly with respect to the wavelength, following the band diagram (Fig. 2i) with dispersion $\frac{d\theta}{d\lambda} = 1.2 \times 10^{-3}$ rad nm^{-1}. Measurements

https://doi.org/10.1038/s41565-023-01360-z

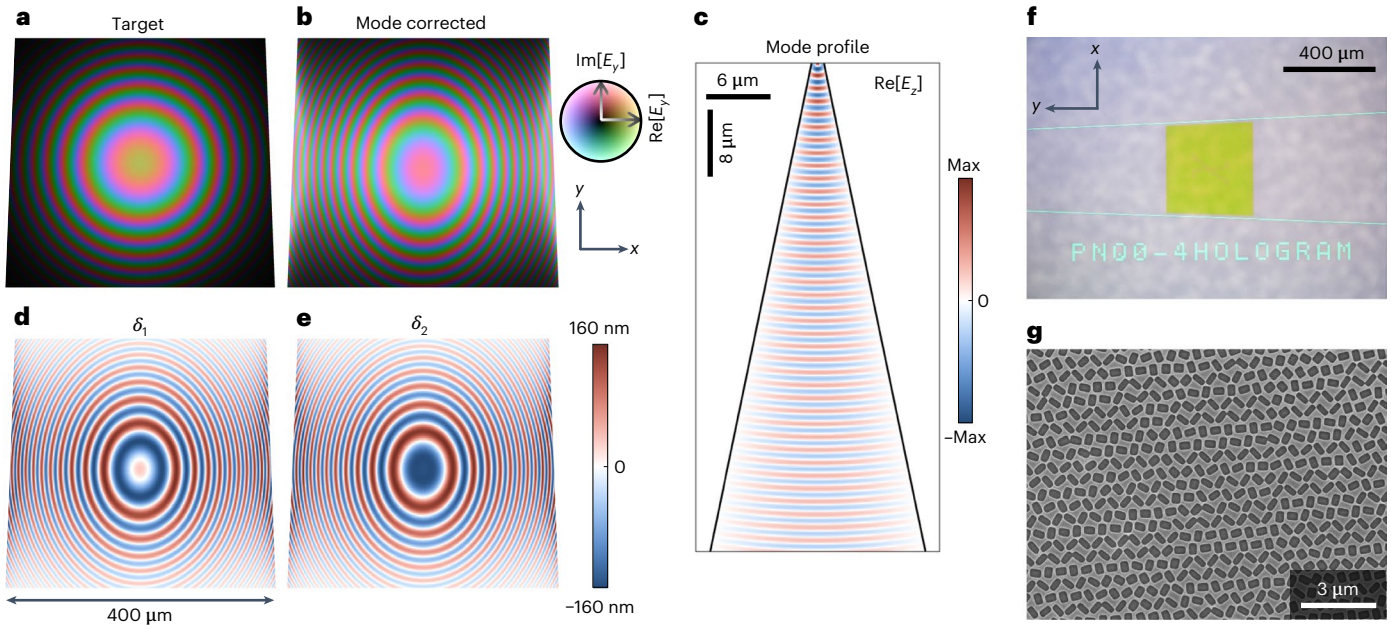

Fig. 4 | Constructing an LWM via modal correction. a, Target PA profiles to produce a converging, linearly polarized beam (*y* polarization). **b**,**c**, Mode-corrected PA profiles (**b**) accounting for the guided-mode PA profiles in **c**. **d**,**e**, Spatial profiles of the perturbation strengths δ_1 (**d**) and δ_2 (**e**), populated based on the map in **b** from the meta-unit library. **f**, Optical micrograph of a fabricated device. **g**, Scanning electron micrograph of the fabricated device.

confirming the linearly polarized radiation of this device are shown in Supplementary Section 7.

Next, Fig. 5f shows a schematic of an LWM generating a vortex beam with OAM order $\ell = 2$, in tandem with a tilted wave with a Gaussian profile that serves as an interferometric reference beam (encoded in the complex near field shown in Fig. 5g). An image taken at $z = 2$ mm shows the interference of the two beams (Fig. 5h), where a characteristic fork pattern with two branches is formed (confirming the OAM order), whereas an image taken at $z = 10$ mm shows the separation of the two beams (Fig. 5i). As another example, Fig. 5j demonstrates a two-image holographic LWM encoded by the two degrees of freedom inherent in a PA metasurface (the complex near field shown in Fig. 5k). The first image—the CUNY logo—is applied as the amplitude profile of the hologram, whereas the second image—the Columbia Engineering logo—is encoded in the phase profile of the hologram (using the Gerchberg–Saxton algorithm[50]) such that the logo is reconstructed at a distance of $z = 1$ mm (NA ≈ 0.2). Images taken at the LWM plane ($z = 0$ mm) and the holographic image plane ($z = 1$ mm) are shown in Fig. 5l and Fig. 5m, respectively.

Finally, as a demonstration of the polarization control of our platform, Fig. 5n depicts an LWM producing a kagome lattice for *x*-polarized light via the complex near-field distribution shown in Fig. 5o (Fig. 5p shows the central region of this distribution). Here the selection rules for the case of $\alpha_1 = \alpha_2 = 45°$ forbids emission to *y* polarization, but allows emission to *x* polarization. The measured result at a plane $z = 0.5$ mm away from the LWM (effective NA ≈ 0.37) is shown in Fig. 5q. Additional devices are reported in Supplementary Sections 7 and 8, including an *x*-polarized Fresnel lens, a device generating radially polarized surface emission and an *x*-polarized two-image hologram to demonstrate complete mastery over linear polarization. The evolution of optical intensity distributions from the LWM plane to the holographic image plane is shown in Supplementary Section 10.

Vector-beam generation

Next, all the four geometric degrees of freedom ($\delta_1, \delta_2, \alpha_1, \alpha_2$) are utilized to realize simultaneous PA control for the two orthogonal polarization components (that is, the PA profile of a vector beam). Figure 6a,b shows a schematic of the four-image holographic LWM, extending the scheme shown in Fig. 5j–m. Images of the letters 'ψ' and 'χ' are applied to the amplitude profiles of the *y* and *x* polarization components of the scattered field, whereas the phase profiles at the two orthogonal polarizations encode the letters '*A*' and 'Φ', respectively, for reconstruction at a distance of $z = 1$ mm (Fig. 6a,b). Images taken at the holographic image plane ($z = 1$ mm) and LWM plane ($z = 0$ mm) for *y* polarization are shown in Fig. 6c and Fig. 6d, respectively; Fig. 6e,f depicts the same data for *x* polarization.

Finally, Fig. 6g shows a schematic of an LWM generating a focused Poincaré beam with the minimum waist size at a distance of $z = 2$ mm (NA ≈ 0.1). Here we implement the Poincaré beam as the superposition of a focused left-circularly polarized (LCP) Gaussian beam and a focused right-circularly polarized (RCP) vortex beam with $\ell = 1$, so that a transverse cross section of the beam reveals all the polarization states over the Poincaré sphere (Fig. 6g). The four optical degrees of freedom that we control in this specific demonstration are the PA profiles of the LCP and RCP states. Figure 6h shows the measured intensity distributions at a distance of $z = 2$ mm and at the six characteristic polarization states, in good agreement with the simulated results (Fig. 6i). The detailed near-field and geometry profiles of the reported devices are summarized in Supplementary Section 9.

Outlook and conclusions

Compared with other techniques, our approach confers a number of advantages originating from the period-doubling perturbation, which exclusively introduces coupling to free space—the mode is otherwise bound. This feature is compatible with large-aperture fields, and here we demonstrated surface emission from integrated devices with a linear dimension that is $>250\lambda_0$. Large-aperture (millimetre scale and above) fields are highly desirable in a number of applications due to their small divergence angles in the far field[51,52]. At the same time, the lattice supports a one-dimensional zone-folded Dirac point, enabling operation at and near the device normal (broadside emission), a feature precluded by the parabolic band structure of modes employed in conventional GC designs. Most importantly, the

https://doi.org/10.1038/s41565-023-01360-z

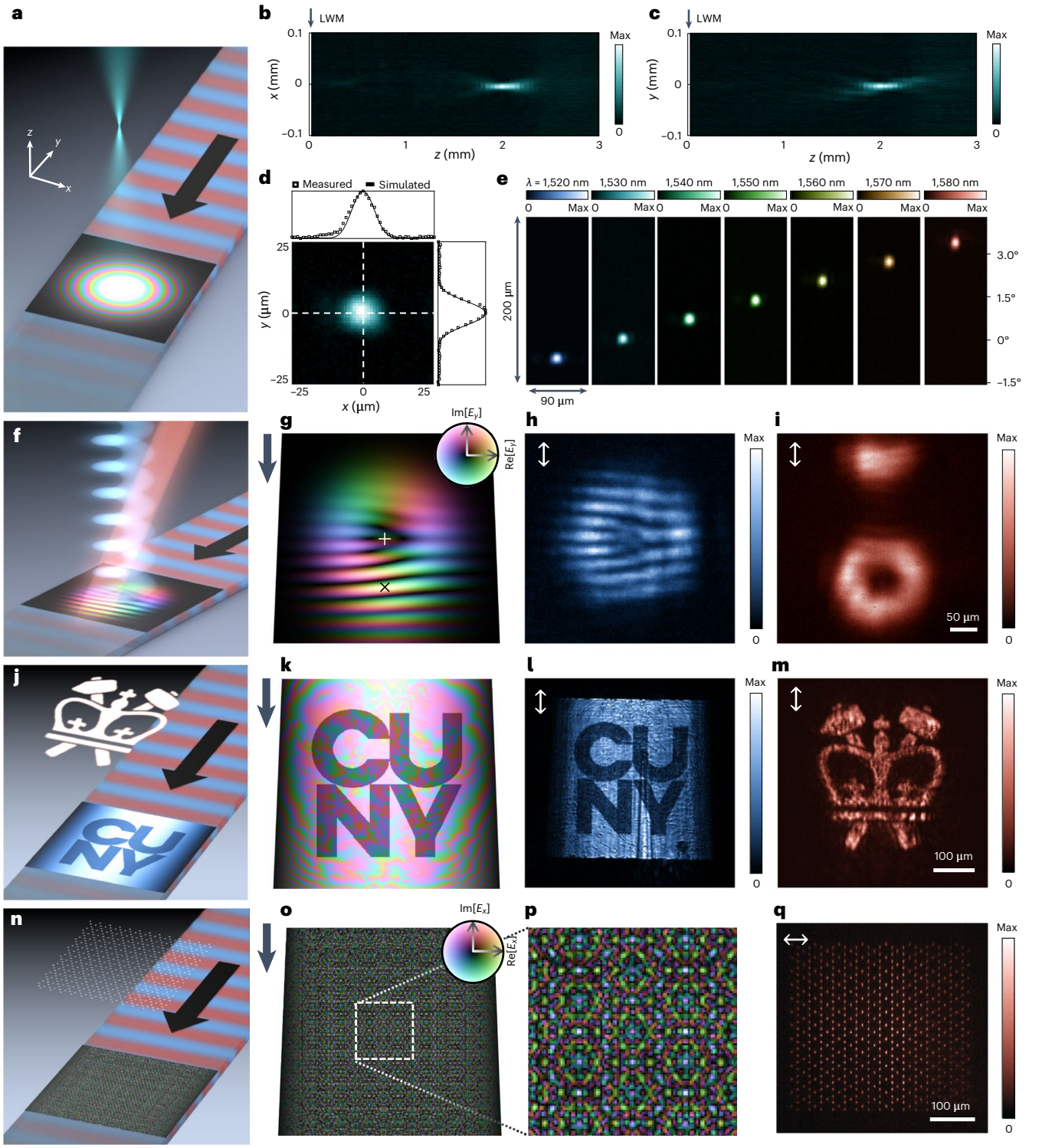

Fig. 5 | PA LWMs for linearly polarized light. a, Schematic of a focusing LWM. **b**,**c**, Measured x–z and y–z cross sections showing focused emission from the LWM at $\lambda_0 = 1{,}550$ nm, with a designed focal length of $f = 2$ mm. **d**, Measured x–y cross section at the focal plane for $\lambda_0 = 1{,}530$ nm, with x and y linecuts compared with the simulated responses based on diffraction-limited behaviour. **e**, Measurement of the focal plane at seven selected wavelengths, demonstrating steering in the y direction, following the leaky-wave dispersion. **f**,**g**, Schematic of an LWM producing an OAM beam with $\ell = 2$ (**f**), along with a tilted Gaussian beam as a reference, via the complex near field in **g** excited in the direction indicated by the black arrow (the white plus marks the centre of the OAM beam emission and the black cross marks the centre of the tilted Gaussian beam). **h**, Measured interference of the two beams at plane $z = 2$ mm, showing a characteristic forked pattern. **i**, Measured emission of the OAM device at a plane $z = 10$ mm away from the LWM, where the OAM and Gaussian beams are separated. **j**,**k**, Schematic of a two-image hologram (**j**), where the grey-scale amplitude distribution at the LWM plane serves as the first image, and a distinct holographic image is produced at the second plane based on the phase profile, collectively encoded in the complex near field in **k**. **l**, Measured grey-scale image (CUNY logo) at the LWM plane. **m**, Measured holographic image (Columbia Engineering logo) at a plane $z = 1$ mm away from the LWM. **n**–**p**, Schematic (**n**) of a kagome lattice generator based on the complex near field in **o**; the central region of this field is shown in **p**. **q**, Measured holographic lattice at a plane $z = 0.5$ mm away from the LWM. All the devices generate y-polarized light, except for the kagome lattice generator, which produces x-polarized surface emission.

https://doi.org/10.1038/s41565-023-01360-z

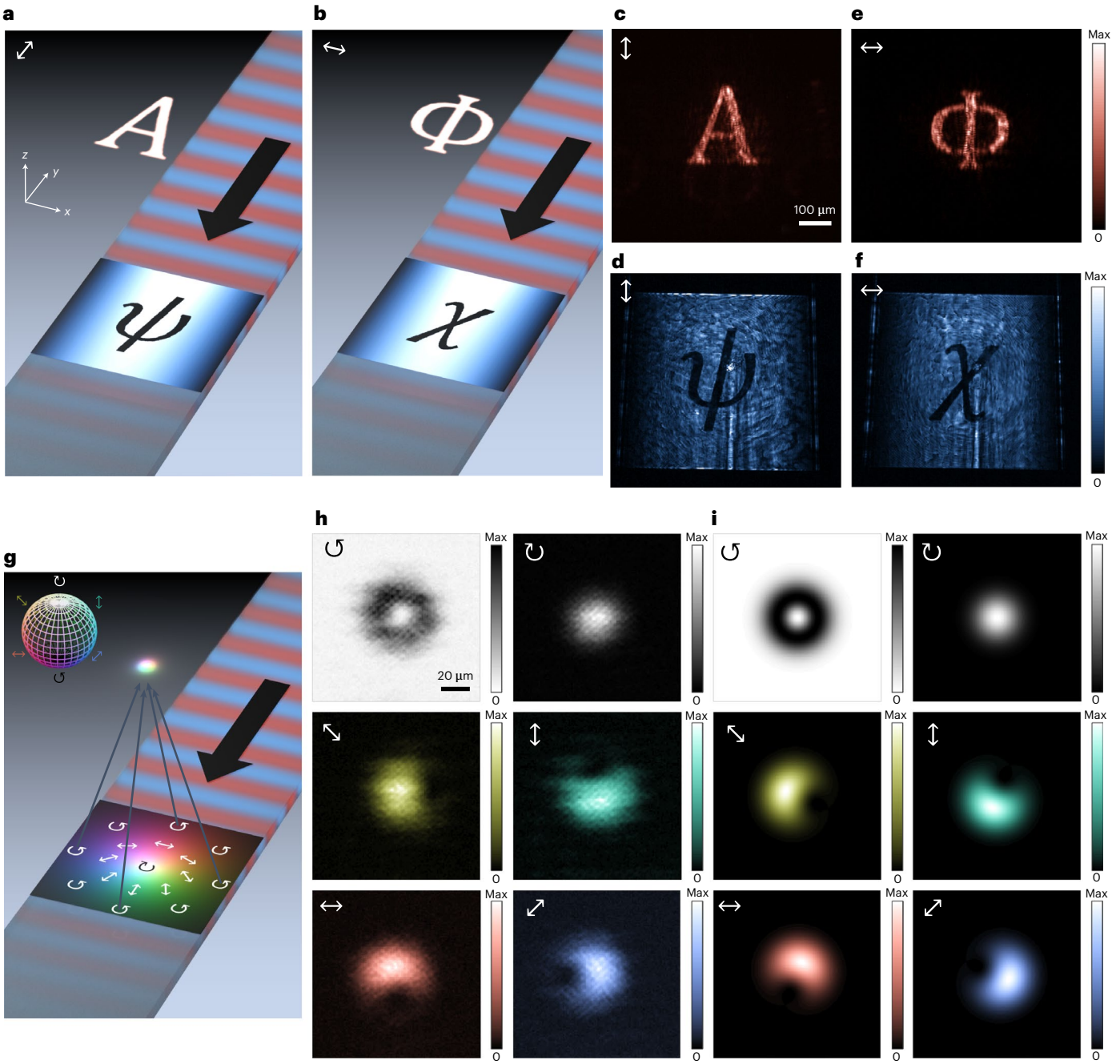

Fig. 6 | Vector-beam LWMs with complete control over amplitude, phase and polarization. a,**b**, Schematic of an LWM producing a four-image hologram, in which two distinct two-image holograms are encoded for *y* (**a**) and *x* (**b**) polarizations. **c**,**d**, Measured *y*-polarized images at the holographic image ($z = 1$ mm; **c**) and LWM plane ($z = 0$ mm; **d**). **e**,**f**, Measured *x*-polarized images at the holographic image plane ($z = 1$ mm; **e**) and LWM plane ($z = 0$ mm; **f**). **g**, Schematic of an LWM producing a focusing Poincaré beam. **h**,**i**, Measured (**h**) and simulated (**i**) profiles of six characteristic polarizations at a plane $z = 2$ mm.

meta-unit motif with two shifted rows of judiciously oriented elliptical apertures enables the simultaneous and independent control of amplitude and polarization state of both real and imaginary components of the LWM radiation: the magnitude of the period-doubling perturbation in each row controls the amplitude of each component, whereas the orientation angle of the perturbation controls the polarization state. The symmetry-driven design enables a semi-analytical mapping between the optical degrees of freedom (A, Φ, ψ, χ) and the geometric design parameters $(\delta_1, \delta_2, \alpha_1, \alpha_2)$. Traditionally, the difficulty in constructing a meta-unit library compounds unfavourably as the number of targeted optical degrees of freedom is increased. Here, in contrast, the LWM geometry is populated in a point-by-point manner based on a set of simple equations, while achieving complete control over the vectorial field.

Building on these advantages, several improvements and extensions may be made to this platform (Supplementary Sections 11–13). In particular, future work may improve the efficiency of the approach by engineering the profile of the scattering strength along the LWM, with near-unity efficiency achievable in suitable designs[53,54]. Our symmetry-based design principle implies that applications involving a wide array of materials and frequencies may adopt this approach. For instance, RF leaky-wave antennas are well known for beamforming and scanning in the far field, but are difficult to operate at close range. Our approach may be used to create RF leaky-wave antennas that operate

across a wide range of distances, and with distinct functionalities imparted to orthogonal polarizations, useful for polarization-division multiplexing. Similarly, in the context of PICs, although here we showed one popular materials platform based on Si_3N_4, the design principle can be applied to silicon-on-insulator technologies. Active materials such as lithium niobate, two-dimensional materials and liquid crystals may also be incorporated, to switch on or off the symmetry-breaking perturbation or to control its magnitude. Finally, although our LWMs are composed of two-dimensional arrays of holes in a thin film, sub-wavelength grating waveguides[55] composed of pillars may also be used based on the same principles.

In conclusion, we have introduced an LWM platform that generates custom vectorial fields at will, combining the functionality of metasurfaces with the compact form factor of GCs. We demonstrated the semi-analytical generation of a library of meta-units with complete command over amplitude, phase and polarization state of light with subwavelength resolution. The design principles are rooted in the symmetries of quasi-bound waves supported by high-symmetry lattices and are thus compatible with a wide range of materials platforms and frequencies. In the future, we anticipate a number of applications stemming from this approach. Our platform may be integrated with PICs for off-chip communications such as chip-to-chip communications and free-space mode-division multiplexing (for example, using OAM (Fig. 5f–i) or Poincaré beams (Fig. 6g–i)), and it may be used to generate custom cold-atom traps for quantum applications (such as kagome lattices (Fig. 5n–q)). Although our implementation employs structural birefringence as a perturbation, small changes in material birefringence (such as in liquid crystals) may achieve similar control but in a dynamic manner. In this way, our approach may also enable LIDAR systems with optically large apertures for arbitrary beamforming (including broadside emission) and beam steering (Fig. 5e), as well as novel holographic display technologies (Fig. 5j–m and Fig. 6a–f).

Online content

Any methods, additional references, Nature Portfolio reporting summaries, source data, extended data, supplementary information, acknowledgements, peer review information; details of author contributions and competing interests; and statements of data and code availability are available at https://doi.org/10.1038/s41565-023-01360-z.

References

1. Yu, N. et al. Light propagation with phase discontinuities: generalized laws of reflection and refraction. *Science* **334**, 333–337 (2011).
2. Yu, N. & Capasso, F. Flat optics with designer metasurfaces. *Nat. Mater.* **13**, 139–150 (2014).
3. Lalanne, P., Astilean, S., Chavel, P., Cambril, E. & Launois, H. Blazed binary subwavelength gratings with efficiencies larger than those of conventional échelette gratings. *Opt. Lett.* **23**, 1081–1083 (1998).
4. Chen, S., Liu, W., Li, Z., Cheng, H. & Tian, J. Metasurface-empowered optical multiplexing and multifunction. *Adv. Mater.* **32**, 1805912 (2020).
5. Kim, M., Wong, A. M. H. & Eleftheriades, G. V. Optical Huygens' metasurfaces with independent control of the magnitude and phase of the local reflection coefficients. *Phys. Rev. X* **4**, 041042 (2014).
6. Overvig, A. C. et al. Dielectric metasurfaces for complete and independent control of the optical amplitude and phase. *Light. Sci. Appl.* **8**, 92 (2019).
7. Arbabi, A., Horie, Y., Bagheri, M. & Faraon, A. Dielectric metasurfaces for complete control of phase and polarization with subwavelength spatial resolution and high transmission. *Nat. Nanotechnol.* **10**, 937–943 (2015).
8. Mueller, J. B., Rubin, N. A., Devlin, R. C., Groever, B. & Capasso, F. Metasurface polarization optics: independent phase control of arbitrary orthogonal states of polarization. *Phys. Rev. Lett.* **118**, 113901 (2017).
9. Bao, Y., Ni, J. & Qiu, C. W. A minimalist single-layer metasurface for arbitrary and full control of vector vortex beams. *Adv. Mat.* **32**, 1905659 (2020).
10. Deng, Z. L. et al. Full-color complex-amplitude vectorial holograms based on multi-freedom metasurfaces. *Adv. Func. Mat.* **30**, 1910610 (2020).
11. Liu, M. et al. Multifunctional metasurfaces enabled by simultaneous and independent control of phase and amplitude for orthogonal polarization states. *Light. Sci. Appl.* **10**, 107 (2021).
12. Wu, T. et al. Dielectric metasurfaces for complete control of phase, amplitude, and polarization. *Adv. Opt. Mater.* **10**, 2101223 (2022).
13. Bao, Y., Wen, L., Chen, Q., Qiu, C. W. & Li, B. Toward the capacity limit of 2D planar Jones matrix with a single-layer metasurface. *Sci. Adv.* **7**, eabh0365 (2021).
14. Svirko, Y., Zheludev, N. & Osipov, M. Layered chiral metallic microstructures with inductive coupling. *Appl. Phys. Lett.* **78**, 498–500 (2010).
15. Kanda, N., Konishi, K. & Kuwata-Gonokami, M. Terahertz wave polarization rotation with double layered metal grating of complimentary chiral patterns. *Opt. Express* **15**, 11117–11125 (2007).
16. Epstein, A. & Eleftheriades, G. V. Arbitrary antenna arrays without feed networks based on cavity-excited omega-bianisotropic metasurfaces. *IEEE Trans. Antennas Propag.* **65**, 1749–1756 (2017).
17. Ra'di, Y., Asadchy, V. S. & Tretyakov, S. A. Tailoring reflections from thin composite metamirrors. *IEEE Trans. Antennas Propag.* **62**, 3749–3760 (2014).
18. Yuan, Y. et al. Independent phase modulation for quadruplex polarization channels enabled by chirality-assisted geometric-phase metasurfaces. *Nat. Commun.* **11**, 4186 (2020).
19. Tamir, T. & Oliner, A. A. Guided complex waves. Part 1: Fields at an interface. *Proc. Inst. Electr. Eng.* **110**, 310–324 (1963).
20. Tamir, T. & Oliner, A. A. Guided complex waves. Part 2: Relation to radiation patterns. *Proc. Inst. Electr. Eng.* **110**, 325–334 (1963).
21. Jackson, D. R. & Oliner, A. A. A leaky-wave analysis of the high-gain printed antenna configuration. *IEEE Trans. Antennas Propag.* **36**, 905–910 (1988).
22. Jackson, D. R. & Oliner, A. A. Leaky-wave antennas. in *Modern Antenna Handbook* (ed Balanis, C. A.) 325–367 (Wiley, 2008).
23. Li, A., Singh, S. & Sievenpiper, D. Metasurfaces and their applications. *Nanophotonics* **7**, 989–1011 (2018).
24. Monticone, F. & Alù, A. Leaky-wave theory, techniques, and applications: from microwaves to visible frequencies. *Proc. IEEE* **103**, 793–821 (2015).
25. Minatti, G., Caminita, F., Casaletti, M. & Maci, S. Spiral leaky-wave antennas based on modulated surface impedance. *IEEE Trans. Antennas Propag.* **59**, 4436–4444 (2011).
26. Tierney, B. B. & Grbic, A. Controlling leaky waves with 1-D cascaded metasurfaces. *IEEE Trans. Antennas Propag.* **66**, 2143–2146 (2018).
27. Abdo-Sánchez, E., Chen, M., Epstein, A. & Eleftheriades, G. V. A leaky-wave antenna with controlled radiation using a bianisotropic Huygens' metasurface. *IEEE Trans. Antennas Propag.* **67**, 108–120 (2018).
28. Meng, Y. et al. Optical meta-waveguides for integrated photonics and beyond. *Light. Sci. Appl.* **10**, 235 (2021).
29. Li, Z. et al. Controlling propagation and coupling of waveguide modes using phase-gradient metasurfaces. *Nat. Nanotechnol.* **12**, 675–683 (2017).

30. Guo, X., Ding, Y., Chen, X., Duan, Y. & Ni, X. Molding free-space light with guided wave-driven metasurfaces. *Sci. Adv.* **6**, eabb4172 (2020).
31. Xie, C. et al. Bifocal focusing and polarization demultiplexing by a guided wave-driven metasurface. *Opt. Express* **29**, 25709–25719 (2021).
32. Huang, Z., Marks, D. L. & Smith, D. R. Out-of-plane computer-generated multicolor waveguide holography. *Optica* **6**, 119–124 (2019).
33. Fang, B., Wang, Z., Gao, S., Zhu, S. & Li, T. Manipulating guided wave radiation with integrated geometric metasurface. *Nanophotonics* **11**, 1923–1930 (2022).
34. Ding, Y. et al. Metasurface-dressed two-dimensional on-chip waveguide for free-space light field manipulation. *ACS Photonics* **9**, 398–404 (2022).
35. Li, L., Yao, K., Wang, Z. & Liu, Y. Harnessing evanescent waves by bianisotropic metasurfaces. *Laser Photonics Rev.* **14**, 1900244 (2020).
36. Ha, Y. et al. Monolithic-integrated multiplexed devices based on metasurface-driven guided waves. *Adv. Theory Simul.* **4**, 2000239 (2021).
37. Yang, R. et al. Immersive tuning the guided waves for multifunctional on-chip metaoptics. *Laser Photonics Rev.* **16**, 2200127 (2022).
38. Shi, Y. et al. On-chip meta-optics for semi-transparent screen display in sync with AR projection. *Optica* **9**, 670–676 (2022).
39. Yulaev, A. et al. Metasurface-integrated photonic platform for versatile free-space beam projection with polarization control. *ACS Photonics* **6**, 2902–2909 (2019).
40. Koshelev, K., Lepeshov, S., Liu, M., Bogdanov, A. & Kivshar, Y. Asymmetric metasurfaces with high-Q resonances governed by bound states in the continuum. *Phys. Rev. Lett.* **121**, 193903 (2018).
41. Overvig, A. C., Malek, S. C., Carter, M. J., Shrestha, S. & Yu, N. Selection rules for quasibound states in the continuum. *Phys. Rev. B* **102**, 035434 (2020).
42. Overvig, A. C., Malek, S. C. & Yu, N. Multifunctional nonlocal metasurfaces. *Phys. Rev. Lett.* **125**, 017402 (2020).
43. Overvig, A., Yu, N. & Alù, A. Chiral quasi-bound states in the continuum. *Phys. Rev. Lett.* **126**, 073001 (2021).
44. Overvig, A. & Alù, A. Diffractive nonlocal metasurfaces. *Laser Photonics Rev.* **16**, 2100633 (2022).
45. Lawrence, M. et al. High quality factor phase gradient metasurfaces. *Nat. Nanotechnol.* **15**, 956–961 (2020).
46. Beckley, A. M., Brown, T. G. & Alonso, M. A. Full Poincaré beams. *Opt. Express* **18**, 10777–10785 (2010).
47. Overvig, A. C., Shrestha, S. & Yu, N. Dimerized high contrast gratings. *Nanophotonics* **7**, 1157–1168 (2018).
48. Memarian, M. & Eleftheriades, G. V. Dirac leaky-wave antennas for continuous beam scanning from photonic crystals. *Nat. Commun.* **6**, 5855 (2015).
49. Overvig, A., Kasahara, Y., Xu, G. & Alù, A. Demonstration of a polarization-agnostic geometric phase in nonlocal metasurfaces. Preprint at http://arxiv.org/abs/2302.13215 (2023).
50. Gerchberg, R. W. & Saxton, W. O. A practical algorithm for the determination of the phase from image and diffraction plane pictures. *Optik* **35**, 237–246 (1972).
51. Poulton, C. V. et al. Large-scale silicon nitride nanophotonic phase arrays at infrared and visible wavelengths. *Opt. Lett.* **42**, 21–24 (2017).
52. Chauhan, N. et al. Photonic integrated Si_3N_4 ultra-large-area grating waveguide MOT interface for 3D atomic clock laser cooling. In *2019 Conference on Lasers and Electro-Optics (CLEO)* STu4O.3 (IEEE, 2019).
53. Bates, K. A., Li, L., Roncone, R. L. & Burke, J. J. Gaussian beams from variable groove depth grating couplers in planar waveguides. *Appl. Opt.* **32**, 2112–2116 (1993).
54. Zhao, Z. & Fan, S. Design principles of apodized grating couplers. *J. Light. Technol.* **38**, 4435–4446 (2020).
55. Cheben, P., Halir, R., Schmid, J. H., Atwater, H. A. & Smith, D. R. Subwavelength integrated photonics. *Nature* **560**, 565–572 (2018).

Methods

Modelling and simulations of meta-units

The Jones vector response of a half meta-unit composed of one pair of ellipses, and excited by a TM slab waveguide mode approximately follows

$$\begin{pmatrix} E_x \\ E_y \end{pmatrix} = \delta \begin{pmatrix} a_x \sin\alpha \\ a_y \cos\alpha \end{pmatrix}, \quad (2)$$

where a_x (a_y) is the maximum amplitude in x (y) polarization, which is achieved at the maximum δ and $\alpha = 45°$ ($\alpha = 0°$). The imbalance between a_x and a_y originates from the asymmetry between the x and y directions of the system. Here only the first-order perturbation effect is considered; in this regime, the dependence on δ is approximately linear. If the meta-unit is instead excited by a transverse-electric slab waveguide mode, the Jones vector response will be rotated 90° due to the conversion between electric field and magnetic field, with an additional constant term in E_x to account for zeroth-order scattering.

Amplitude A and polarization orientation angle ψ of a half meta-unit can be independently controlled by geometric parameters δ and α, respectively. For given target values of A and ψ, the corresponding geometric parameters can be explicitly solved:

$$\alpha = \frac{1}{2}\mathrm{arc}\left(\frac{a_y}{a_x}\tan\psi\right), \quad (3)$$

$$\delta = \frac{A}{a_y}\cos\psi\sqrt{1+\left(\frac{a_y}{a_x}\tan\psi\right)^2}. \quad (4)$$

For a full meta-unit composed of two pairs of $p2$ ellipses displaced by a quarter period along the propagation direction, the response is a coherent summation of the two pairs with a 90° phase difference:

$$\begin{pmatrix} E_x \\ E_y \end{pmatrix} = \delta_1 \begin{pmatrix} a_x \sin\alpha_1 2 \\ a_y \cos\alpha_1 2 \end{pmatrix} + i\delta_2 \begin{pmatrix} a_x \sin\alpha_2 2 \\ a_y \cos\alpha_2 2 \end{pmatrix}, \quad (5)$$

where the first pair of ellipses (characterized by (δ_1, α_1)) contributes to the real part and the second pair of ellipses (characterized by (δ_2, α_2)) contributes to the imaginary part. For a complex target $(E_x, E_y)^T$, the required geometric parameters can be solved by first calculating the amplitudes $A_{1,2}$ and polarization orientation angles $\psi_{1,2}$ of the real and imaginary parts, respectively:

$$A_1 = \sqrt{[\mathrm{Re}(E_x)^2] + [\mathrm{Re}(E_y)^2]}, \quad (6)$$

$$A_2 = \sqrt{[\mathrm{Im}(E_x)^2] + [\mathrm{Im}(E_y)^2]}, \quad (7)$$

$$\psi_1 = \mathrm{arc}\tan\frac{\mathrm{Re}(E_x)}{\mathrm{Re}(E_y)}, \quad (8)$$

$$\psi_2 = \mathrm{arc}\tan\frac{\mathrm{Im}(E_x)}{\mathrm{Im}(E_y)}, \quad (9)$$

and then using the above formulas derived for each half meta-unit:

$$\alpha_{1,2} = \frac{1}{2}\mathrm{arc}\left(\frac{a_y}{a_x}\tan\psi_{1,2}\right), \quad (10)$$

$$\delta_{1,2} = \frac{A_{1,2}}{a_y}\cos\psi_{1,2}\sqrt{1+\left(\frac{a_y}{a_x}\tan\psi_{1,2}\right)^2}. \quad (11)$$

Finite-difference time-domain simulation results of the polarization ellipticity angle (χ) and polarization orientation angle (ψ) of a leaky-wave meta-unit are shown in Fig. 3e,f, where α_1 and α_2 are swept from 0° to 90° to cover the polarization space, and $\delta_{1,2}$ are set according to $\alpha_{1,2}$ to generate a flat amplitude response. A full coverage of the polarization ellipticity angle from $\chi = +\pi/4$ (LCP) through $\chi = 0$ (linear polarization) to $\chi = -\pi/4$ (RCP) is achieved as $\alpha_1 - \alpha_2$ varies from +45° through 0° to −45° (Fig. 2f), and a full coverage of the polarization orientation angle from $\psi = -\pi/2$ to $\psi = +\pi/2$ is achieved as α_1 and α_2 vary from 0° to 90° in the $|\alpha_1 - \alpha_2| < 45°$ region (Fig. 3e). Further simulation results of amplitude (A) and phase (Φ) responses are shown in Fig. 3b and Fig. 3c, respectively, where $\alpha_1 = \alpha_2 = 0°$ is set to fix the polarization at $\chi = \psi = 0$ (y polarized). Full coverage of PA is achieved along the radial (Fig. 3b) and azimuthal (Fig. 3c) directions in the parameter sweep, respectively.

Note that this approach assumes that the slab waveguide mode travels along the $-y$ direction, regardless of the position across the device. Supplementary Sections 6 and 12 discuss and justify this assumption in more detail, showing that even at the boundaries of the tapered slab waveguide, where the local propagation direction of the guided wave has the largest deviation (~2.4°) from the $-y$ direction, the change in device performance is negligible. In cases where the above assumption fails, a conformal transformation of the lattice geometry could be explored to align the local lattice parameters with the local guided mode's propagation direction.

The meta-unit responses are simulated via the finite-difference time-domain method (Lumerical). An array of $N = 9$ identical meta-units are placed along the y direction with periodic x boundaries and perfectly matched layers at the y and z boundaries. A total-field/scattered-field source is launched in the $-z$ direction, and a mode expansion monitor is placed on the $-y$ side to calculate the complex amplitude of the generated fundamental TM slab waveguide mode. Two separate simulations with x- and y-polarized total-field/scattered-field sources are performed to obtain the E_x and E_y responses, respectively.

Device fabrication

We experimentally demonstrate LWMs at the telecommunications wavelength ($\lambda \approx 1.55$ μm) using a polymer–Si_3N_4 materials platform. The waveguide circuit and the meta-unit holes composing the metasurface are patterned in a 300 nm poly(methyl methacrylate) layer, on the top of a 300 nm Si_3N_4 thin film, on a SiO_2 substrate. The fundamental TM guided mode is fed from a single-mode ridge waveguide via a linear taper with a tapering rate of $\Delta w/\Delta L = 1/12$. An LWM device with a linear dimension of ~400 μm is integrated within the taper (Fig. 4f). The PA distributions in the tapered slab waveguide are non-uniform, which should be compensated for when designing the LWM PA profiles. Expanded from a single-mode waveguide through a linear taper, the slab waveguide mode can be approximated with an analytic expression:

$$E(x,y) = E_0 A(x,y) e^{i\phi(x,y)}, \quad (12)$$

with

$$A(x,y) = \sqrt{\frac{w_0}{w(y)}}\cos\left[\frac{\pi x}{w(y)}\right] e^{\frac{\alpha y}{2}}, \quad (13)$$

$$\phi(x,y) = \frac{2\pi}{\lambda}\left[-n_{ms}y + n_{wg}\frac{x^2}{2(L-y)}\right], \quad (14)$$

where the amplitude distribution $A(x, y)$ is formed by the collective effects of (1) waveguide widening, that is, $w(y) = w_0 + \Delta w/\Delta L \times (L - y)$, where $L \approx 4{,}800$ μm is the taper length and y is the longitudinal coordinate; (2) transverse waveguide mode profile associated with the local waveguide width $w(y)$; and (3) attenuation due to out-coupling

from the metasurface; the phase distribution $\phi(x, y)$ is composed of (1) longitudinal phase accumulation in the metasurface region with an effective modal index $n_{ms} \approx 1.52$ and (2) transversal phase profile in the linear taper with an effective modal index $n_{wg} \approx 1.55$, approximated by a paraxial cylindrical wave.

Finally, the devices are fabricated as follows. Si_3N_4 thin films with 300 nm thickness are grown via plasma-enhanced chemical vapour deposition on a fused silica substrate of 180 µm thickness. A 300 nm poly(methyl methacrylate) layer is spin coated and baked at 180 °C to serve as an electron-beam resist. Electron-beam lithography (Elionix ELS-G100) is then carried out at 100 keV and 1 nA, with a dose of 750 µC cm^{-2} and appropriate proximity effect corrections (BEAMER), to define the waveguide boundaries and LWM patterns. A 3:1 mixture of isopropyl alcohol and deionized water is used to develop the exposed resist. The fabricated chip is then cleaved to expose the facet of the narrow single-mode ridge waveguide for fibre coupling.

Device characterization

Near-infrared light at $\lambda \approx 1.55$ µm is generated by a diode laser, and coupled into the LWM device using a lensed optical fibre with proper polarization adjustment. The surface emission on the air side produced by the device is collected by a ×10 or ×20 near-infrared objective (Mitutoyo), passed through a polarization filter (Thorlabs) and directed towards a near-infrared camera (Princeton Instruments).

Data availability

All relevant data are available within the Article and its Supplementary Information.

Acknowledgements

This work was supported by the National Science Foundation (grant no. QII-TAQS-1936359 (H.H., Y.X. and N.Y.) and no. ECCS-2004685 (S.C.M., C.-C.T. and N.Y.)), the Air Force Office of Scientific Research (grant no. FA9550-16-1-0322 (N.Y.), no. FA9550-18-1-0379 (A.C.O. and A.A.) and no. FA9550-21-1-0312 (A.C.O. and A.A.)), a Vannevar Bush Faculty Fellowship (A.C.O and A.A.) and the Simons Foundation (A.C.O. and A.A). S.C.M. acknowledges support from the NSF Graduate Research Fellowship Program (grant no. DGE-1644869). Device fabrication was carried out at the Columbia Nano Initiative cleanroom, and at the Advanced Science Research Center NanoFabrication Facility at the Graduate Center of the City University of New York.

Author contributions

A.C.O., H.H. and N.Y. conceived the idea. H.H. and A.C.O. mathematically modelled the devices and performed the simulations. H.H. designed and fabricated the devices. H.H., A.C.O., Y.X., S.C.M., C.-C.T. and N.Y. characterized the devices. A.C.O. and H.H. analysed the data. A.C.O., H.H., A.A. and N.Y. wrote the manuscript. A.A. and N.Y. supervised the research.

Competing interests

A.C.O., S.C.M. and N.Y. are listed as inventors in a US non-provisional patent application no. 17/110,846; in addition, H.H., Y.X., A.C.O., A.A. and N.Y. are listed as inventors in a US provisional patent application no. 63/342,475. Both were filed by Columbia University and are related to the technology reported in this Article. The remaining authors declare no competing interests.

Additional information

Supplementary information The online version contains supplementary material available at https://doi.org/10.1038/s41565-023-01360-z.

Correspondence and requests for materials should be addressed to Andrea Alù or Nanfang Yu.

Peer review information *Nature Nanotechnology* thanks Vladimir Aksyuk and Yongmin Liu for their contribution to the peer review of this work.